

Spectroscopic super-resolution fluorescence cell imaging using ultra-small Ge quantum dots

MINGYING SONG,^{1,*} ALI KARATUTLU,^{1,2} ISMA ALI,³ OSMAN ERSOY,¹ YUN ZHOU,⁴ YONGXIN YANG,⁴ YUANPENG ZHANG,¹ WILLIAM R. LITTLE,¹ ANN P. WHEELER,⁵ AND ANDREI V. SAPELKIN¹

¹*School of Physics and Astronomy, Queen Mary University of London, London E1 4NS, UK*

²*Electrical and Electronic Engineering, Bursa Orhangazi University, Bursa 16310, Turkey*

³*Nikon Imaging Centre, King's College London, UK*

⁴*School of Electronic Engineering and Computer Science, Queen Mary University of London, London E1 4NS, UK*

⁵*Institute of Genetics and Molecular Medicine, University of Edinburgh and Edinburgh Super-Resolution Interdisciplinary Consortium, Edinburgh EH4 2XU, UK*

*m.song@qmul.ac.uk

Abstract: We demonstrate a spectroscopic imaging based super-resolution approach by separating the overlapping diffraction spots into several detectors during a single scanning period and taking advantage of the size-dependent emission wavelength in nanoparticles. This approach has been tested using off-the-shelf quantum dots (Invitrogen Qdot) and in-house novel ultra-small (~ 3 nm) Ge QDs. Furthermore, we developed a method-specific Gaussian fitting and maximum likelihood estimation based on a Matlab algorithm for fast QD localisation. This methodology results in a three-fold improvement in the number of localised QDs compared to non-spectroscopic images. With the addition of advanced ultra-small Ge probes, the number can be improved even further, giving at least 1.5 times improvement when compared to Qdots. Using a standard scanning confocal microscope we achieved a data acquisition rate of 200 ms per image frame. This is an improvement on single molecule localisation super-resolution microscopy where repeated image capture limits the imaging speed, and the size of fluorescence probes limits the possible theoretical localisation resolution. We show that our spectral deconvolution approach has a potential to deliver data acquisition rates on the ms scale thus providing super-resolution in live systems.

Published by The Optical Society under the terms of the [Creative Commons Attribution 4.0 License](#). Further distribution of this work must maintain attribution to the author(s) and the published article's title, journal citation, and DOI.

OCIS codes: (160.4236) Nanomaterials; (180.1790) Confocal microscopy; (180.2520) Fluorescence microscopy; (110.2960) Image analysis; (100.6640) Superresolution.

References and links

1. P. Xi, Y. Liu, and Q. Ren, "Scanning and Image Reconstruction Techniques in Confocal Laser Scanning Microscopy," in *Laser Scanning, Theory and Application*, C.C. Wang, ed. (Shanghai: InTech, 2011).
2. R. Heintzmann and G. Ficz, "Breaking the resolution limit in light microscopy," *Brief. Funct. Genomics Proteomics* **5**(4), 289–301 (2006).
3. C. Cremer, *Optics Far Beyond the Diffraction Limit*, 2nd edition (Springer, 2012), Chapter 20.
4. M. G. L. Gustafsson, "Nonlinear structured-illumination microscopy: wide-field fluorescence imaging with theoretically unlimited resolution," *Proc. Natl. Acad. Sci. U.S.A.* **102**(37), 13081–13086 (2005).
5. M. Schrader and S. W. Hell, "4Pi confocal images with axial super-resolution," *J. Microsc.* **183**(08), 189–195 (1996).
6. S. W. Hell and J. Wichmann, "Breaking the diffraction resolution limit by stimulated emission: stimulated-emission-depletion fluorescence microscopy," *Opt. Lett.* **19**(11), 780–782 (1994).
7. M. J. Rust, M. Bates, and X. Zhuang, "Sub-diffraction-limit imaging by stochastic optical reconstruction microscopy (STORM)," *Nat. Methods* **3**(10), 793–796 (2006).

8. E. Betzig, G. H. Patterson, R. Sougrat, O. W. Lindwasser, S. Olenych, J. S. Bonifacino, M. W. Davidson, J. Lippincott-Schwartz, and H. F. Hess, "Imaging intracellular fluorescent proteins at nanometer resolution," *Science* **313**(5793), 1642–1645 (2006).
9. P. Lemmer, M. Gunkel, D. Baddeley, R. Kaufmann, A. Urich, Y. Weiland, J. Reymann, P. Müller, M. Hausmann, and C. Cremer, "SPDM: light microscopy with single-molecule resolution at the nanoscale," *Appl. Phys. B* **93**(1), 1–12 (2008).
10. N. A. Hosny, M. Song, J. T. Connelly, S. Ameer-Beg, M. M. Knight, and A. P. Wheeler, "Super-resolution imaging strategies for cell biologists using a spinning disk microscope," *PLoS One* **8**(10), e74604 (2013).
11. D. R. Whelan and T. D. M. Bell, "Super-resolution single-molecule localization microscopy: tricks of the trade," *J. Phys. Chem. Lett.* **6**(3), 374–382 (2015).
12. W. J. Parak, T. Pellegrino, and C. Plank, "Labelling of cells with quantum dots," *Nanotechnology* **16**(2), R9–R25 (2005).
13. A. Small and S. Stahlheber, "Fluorophore localization algorithms for super-resolution microscopy," *Nat. Methods* **11**(3), 267–279 (2014).
14. D. Źurek-Biesiada, A. T. Szczurek, K. Prakash, G. Best, G. K. Mohana, H. K. Lee, J. Y. Roignant, J. W. Dobrucki, C. Cremer, and U. Birk, "Quantitative super-resolution localization microscopy of DNA in situ using Vybrant® DyeCycle™ Violet fluorescent probe," *Data Brief* **7**, 157–171 (2016).
15. H. Arya, Z. Kaul, R. Wadhwa, K. Taira, T. Hirano, and S. C. Kaul, "Quantum dots in bio-imaging: Revolution by the small," *Biochem. Biophys. Res. Commun.* **329**(4), 1173–1177 (2005).
16. J. K. Jaiswal, E. R. Goldman, H. Mattoussi, and S. M. Simon, "Use of quantum dots for live cell imaging," *Nat. Methods* **1**(1), 73–78 (2004).
17. X. Michalet, F. F. Pinaud, L. A. Bentolila, J. M. Tsay, S. Doose, J. J. Li, G. Sundaresan, A. M. Wu, S. S. Gambhir, and S. Weiss, "Quantum dots for live cells, in vivo imaging, and diagnostics," *Science* **307**(5709), 538–544 (2005).
18. B. N. Giepmans, T. J. Deerinck, B. L. Smarr, Y. Z. Jones, and M. H. Ellisman, "Correlated light and electron microscopic imaging of multiple endogenous proteins using Quantum dots," *Nat. Methods* **2**(10), 743–749 (2005).
19. M. Bruchez, Jr., M. Moronne, P. Gin, S. Weiss, and A. P. Alivisatos, "Semiconductor nanocrystals as fluorescent biological labels," *Science* **281**(5385), 2013–2016 (1998).
20. E. Tholouli, E. Sweeney, E. Barrow, V. Clay, J. A. Hoyland, and R. J. Byers, "Quantum dots light up pathology," *J. Pathol.* **216**(3), 275–285 (2008).
21. M. F. Frasco and N. Chaniotakis, "Semiconductor quantum dots in chemical sensors and biosensors," *Sensors (Basel)* **9**(9), 7266–7286 (2009).
22. M. A. Walling, J. A. Novak, and J. R. E. Shepard, "Quantum dots for live cell and in vivo imaging," *Int. J. Mol. Sci.* **10**(2), 441–491 (2009).
23. J. Fan and P. K. Chu, "Group IV nanoparticles: synthesis, properties, and biological applications," *Small* **6**(19), 2080–2098 (2010).
24. N. H. Chou, K. D. Oyler, N. E. Motl, and R. E. Schaak, "Colloidal synthesis of germanium nanocrystals using room-temperature benchtop chemistry," *Chem. Mater.* **21**(18), 4105–4107 (2009).
25. H. P. Wu, J. F. Liu, Y. W. Wang, Y. W. Zeng, and J. Z. Jiang, "Preparation of Ge nanocrystals via ultrasonic solution reduction," *Mater. Lett.* **60**(7), 986–989 (2006).
26. J. H. Warner and R. D. Tilley, "Synthesis of water-soluble photoluminescent germanium nanocrystals," *Nanotechnology* **17**(15), 3745–3749 (2006).
27. J. Wilcoxon, P. Provencio, and G. Samara, "Erratum: Synthesis and optical properties of colloidal germanium nanocrystals," *Phys. Rev. B* **76**(19), 199904 (2007).
28. D. C. Lee, J. M. Pietryga, I. Robel, D. J. Werder, R. D. Schaller, and V. I. Klimov, "Colloidal synthesis of infrared-emitting germanium nanocrystals," *J. Am. Chem. Soc.* **131**(10), 3436–3437 (2009).
29. T. Zimmermann, J. Rieddorf, and R. Pepperkok, "Spectral imaging and its applications in live cell microscopy," *FEBS Lett.* **546**(1), 87–92 (2003).
30. E. Lubeck and L. Cai, "Single-cell systems biology by super-resolution imaging and combinatorial labeling," *Nat. Methods* **9**(7), 743–748 (2012).
31. J. S. Biteen, M. A. Thompson, N. K. Tselentis, G. R. Bowman, L. Shapiro, and W. E. Moerner, "Super-resolution imaging in live Caulobacter crescentus cells using photoswitchable EYFP," *Nat. Methods* **5**(11), 947–949 (2008).
32. K. Lidke, B. Rieger, T. Jovin, and R. Heintzmann, "Superresolution by localization of quantum dots using blinking statistics," *Opt. Express* **13**(18), 7052–7062 (2005).
33. A. J. Williamson, C. Bostedt, T. Van Buuren, T. M. Willey, L. Terminello, G. Galli, and L. Pizzagalli, "Probing the electronic density of states of Germanium nanoparticles," *Nano Lett.* **4**(6), 1041–1045 (2004).
34. X. Liu, M. Atwater, J. Wang, and Q. Huo, "Extinction coefficient of gold nanoparticles with different sizes and different capping ligands," *Colloids Surf. B Biointerfaces* **58**(1), 3–7 (2007).
35. D. Baddeley, Y. Weiland, C. Batram, U. Birk, and C. Cremer, "Model based precision structural measurements on barely resolved objects," *J. Microsc.* **237**(1), 70–78 (2010).
36. A. Karatutlu, M. Song, A. P. Wheeler, O. Ersoy, W. Little, Y. Zhang, P. Puech, F. Boi, Z. Luklinska, and A. V. Sapelkin, "Synthesis and structure of free-standing germanium quantum dots and their application in live cell imaging," *RSC Advances* **5**(26), 20566–20573 (2015).

37. W. R. Funnell and D. Maysinger, "Three-dimensional reconstruction of cell nuclei, internalized quantum dots and sites of lipid peroxidation," *J. Nanobiotechnology* **4**(1), 10 (2006).
38. H. Chen, Y. Gong, and R. Han, "Cadmium telluride quantum dots (CdTe-QDs) and enhanced ultraviolet-B (UV-B) radiation trigger antioxidant enzyme metabolism and programmed cell death in wheat seedlings," *PLoS One* **9**(10), e110400 (2014).
39. R. Neher and E. Neher, "Optimizing imaging parameters for the separation of multiple labels in a fluorescence image," *J. Microsc.* **213**(1), 46–62 (2004).
40. I. Sychugov, R. Juhasz, J. Valenta, and J. Linnros, "Narrow luminescence linewidth of a silicon quantum dot," *Phys. Rev. Lett.* **94**(8), 087405 (2005).
41. K. P. Murphy, *Machine Learning: A Probabilistic Perspective* (Massachusetts Institute of Technology, 2012)
42. A. Buades, B. Col, and J. M. Morel, "A review of image denoising algorithms," *Multiscale Model. Simul.* **5**, 49–53 (2005).
43. L. Zhu, W. Zhang, D. Elnatan, and B. Huang, "Faster STORM using compressed sensing," *Nat. Methods* **9**(7), 721–723 (2012).
44. N. Banterle, K. H. Bui, E. A. Lemke, and M. Beck, "Fourier ring correlation as a resolution criterion for super-resolution microscopy," *J. Struct. Biol.* **183**(3), 363–367 (2013).

1. Introduction

In far-field scanning confocal fluorescence microscopy the imaging resolution has been brought to the diffraction limit (the Abbe diffraction limit) by exclusively collecting the signal at the focal point of an object via a conjugated pinhole before detection [1]. This approach results in lateral resolution of ~200 nm and axial resolution of ~600 nm [2] which is in practice normally measured in terms of the Full Width at Half Maximum (FWHM) of Point Spread Function (PSF) [3]. Super-resolution strategies to break this diffraction limit have been focusing on physically modifying the illumination or increasing the effective numerical aperture (NA) and include methods such as Structured Illumination Microscopy (SIM [4], ~50 nm lateral resolution), 4Pi Microscopy [5] (~100 nm axial resolution) and Simulated Emission Depletion (STED [6], ~20 nm lateral and ~50 nm axial resolution). Another approach is based on temporal separation of emission signals of fluorescent probes followed by precise localisation of a single probe with subsequent image reconstruction, thus achieving higher resolution. These include Stochastic Optical Reconstruction Microscopy (STORM [7], ~20 nm lateral resolution), Photo-activated Localisation Microscopy (PALM [8], ~20 nm lateral resolution), Spectral Precision Distance/Position Determination Microscopy (SPDM [9], ~20 nm lateral and ~50 nm axial resolution), Spinning Disk microscopy for Super-resolution Imaging (SDSI [10], ~30nm lateral resolution). These techniques have achieved an improvement in optical resolution which advanced the optical imaging research of fixed cells, but some limitations still remain. For example, structural illumination based super-resolution methods are technically challenging (e.g extra optical elements, complex system set up etc.) and come at high cost, while providing only moderate improvement in resolution. Localisation methods based on temporal separation of fluorescent probes improve spatial resolution, but are time-consuming which means that the data acquisition can take too long (i.e. 10 minutes). This means the methodologies are suitable only for imaging of fixed cells, as many biological processes occur faster than the time taken to acquire a super-resolution image [10,11].

Besides the optical system itself, the spatial resolution capability in localisation microscopy is determined by probe sizes, labelling density, and reconstruction algorithms. Recent reports [12–14] have demonstrated many precise methods of optimizing labelling density and reconstruction solutions dealing with either sparse fluorescence signals or dense signals. Organic fluorescence probes and chemical dyes which have been commonly used in fluorescence labelling have limited utility as they bleach under repeated illumination, can be cytotoxic and are difficult to directly label to epitopes, are restricted in excitation wavelength to a narrow band, and their emission spectra means they have spectral bleed-through artefacts [15]. Emergence of Quantum dots (QDs, light-emitting nanoparticles) as novel fluorescence probes has been attracting much attention since their applications on live cell imaging [16,17] and in correlative imaging microscopy [18]. QDs are nanoparticles that rely on confinement

of the charge carries (electrons and holes) as the mechanism behind the light emission. The energy gap (that defines the peak emission wavelength) between the HOMO – LUMO energy levels depends on size with smaller size corresponding to the larger energy gap [12,19] and hence the shorter emission wavelength. Small size (generally below ~30 nm), high sensitivities to excitation laser light and relatively high brightness, stable fluorescence emission, stochastic blinking and, in particular, broad excitation and narrow emission [20] makes QDs a perfect hybrid fluorescence label for cell imaging. However, QDs applications in super-resolution cells imaging are still limited by their physical size (localisation resolution limit), toxicity, and cost (complexity of synthesis) [21]. Typically core/shell type II-VI, III-V QDs (e.g CdSe, CdS, CdTe, PbS, InP) are capped (e.g with ZnS) to reduce release of toxic components (i.e. Cd) and coated with transparent biocompatible materials (e.g carboxyl groups) [22]. This results in a total probe size of up to ~50 nm, which limits the localisation resolution. At the same time, group IV QDs (C, Ge, Si) may offer a feasible alternative due to the relatively low toxicity and small size (down to ~1 nm). Ultra-small Ge QDs have recently received a lot of attention because of their good performance in fluorescence imaging [23] and simple synthesis methods [23–26]. Ge QDs of 2-4 nm can be synthesised by easily scalable bench top colloidal route at room temperature yielding the light emission range of 350-700 nm [27], and of 3.2-6.4 nm for the 900-1400 nm light emission [28]. These systems have already been used for live cell imaging applications [23].

Others have made some headway in use of spectral deconvolution – mostly in confocal microscopy to improve resolution. This approach uses fluorescence probes with different peak emission wavelength that are photo-activated and imaged during a single scanning period and fluorescence signals are separated by the emission spectra, per wavelength [29]. This results in the fast data acquisition at frame rates similar to point scanning confocal microscopy (microseconds to seconds) [2,30]. Chemical dyes and proteins have been successfully applied to this method by several groups (Heintzman [2], Cremer [9] and Moerner [31]), particularly when assigning continuous structures or for Fluorescence In Situ Hybridisation. There has been some headway made in using conventional quantum dots to improve resolution beyond the Abbe limit [32]. However because of the large probe size of conventional Qdots (50 nm) the probe size limits effective resolution to between 50 and 200 nm.

Here we propose an approach based on spectroscopic (rather than temporal) separation microscopy using group IV Ge QDs and that takes advantage of QDs size dependent emission spectra to address both the time constraints in temporal separation and physical size limit, and particularly suited for live cell imaging. We tested our approach using off-the-shell Invitrogen CdSe/ZnS based Qdots and in-house synthesised Ge QDs. In this study we show that utilising these new probes together with our novel spectral deconvolution and structural assignment method spatial localisation numbers can be improved at data acquisition rates of 1.6 seconds per super-resolution frame using a standard confocal microscope. This super-resolution microscopy approach is further complemented by specially developed reconstruction algorithm.

2. Methods

2.1 QDs and chemicals

Qdots were purchased from Invitrogen (life Technologies, Qdot Streptavidin Sampler Kit: 525 nm, 605 nm, 705 nm) of 1 μ M solution (50 μ L volume) each in a vial. Dilution and quantitative mixture samples were obtained through calculation based on the labelled parameters. Synthesis of Ge QDs started from original materials GeCl₄, ethylene glycol and 2M of sodium borohydride solution in triethylene glycol dimethyl that were purchased from Sigma-Aldrich, following an optimised bench top-colloidal synthesis route [24]. In order to suspend Ge QDs into different liquid medium, Ge QDs product in colloidal chemical solution

was centrifuged at 10,000 rpm and up layer chemical solution was then removed. Deposited QDs were dried with Ar gas and weighted before re-suspended in a certain amount of water/cell growth medium (usually 10 mg QDs in 1 mL water). Sterilisation was completed by putting the QDs vial under UV light (150mJ/CM², UV CrossLinker) for 15 minutes. When stored in a fridge at 4 °C for a few days, Ge QDs may deposit at the bottom of vial. In this case, QDs could be dispersed by putting the sample into a waterbath sonicator for 12-15 minutes. All QDs were capable to be conjugated to specific binding antibodies.

2.2 Characterisation of Ge QDs

QDs were characterised in optical emission and transmission electron microscope. Emission data were collected using a high resolution spectrometer (Andor Shamrock SR-163) while the QDs samples were excited under a He-Cd 442 nm laser (IK552R-F, Kimmon). Data was collected by Andor Solis software. OriginPro 9.0 was used to plot and analyse these data. In order to measure the size of QDs using TEM, one drop (< 10 µL) of QDs diluted in water was prepared onto a Holey Carbon film Cu grid (300 Mesh, Argar Scientific). It was then allowed to dry in a hood at room temperature for 24 hours. Next, the sample was transferred to the TEM. Images were taken at 50000 × magnification which corresponds to an image pixel size of 9.582 Å. TEM images were analysed in ImageJ 1.46. Sizes data were then plotted in OriginPro 9.0.

2.3 Cell culture

HeLa cells were cultivated in growth medium (89% high glucose DMEM, 10% Foetal Carf Serum and 1% Penicillin, Streptomycin) and maintained at 37 °C with 5% CO₂. Cells were seeded onto glass coverslips at density of 5x10⁴ cells per mL in a 12-well plate and incubated overnight. QDs of concentrations ranging from 20 nM to 500 nM were directly added to HeLa cells for toxicity testing and non-specific fluorescence labelling. Cells were incubated with Qdots for 6 hours prior to experimentation, cells were washed twice with Phosphate Buffered Saline solution (PBS) and then fixed 4% Paraformaldehyde solution (PFA) per well for 10 minutes at room temperature, followed by 3 washes with PBS. Washed coverslips mounted with 5 µL mowiol mounting medium each coverslip and sealed with clear nail polish. All cell-related experiments were repeated in triplicate.

2.4 Calculations and statistical analysis

The density of QDs expressed in molar concentration was determined and calculated following a widely accepted method [33,34]. In this method, the molar concentration of QDs solution is proportional to the total number of atoms while inverse proportional to the production of the number of atoms per QD, solution volume and Avogadro's constant. Statistical analysis for biocompatibility test data was carried out using the OriginPro software package. Unpaired Student's *t*-test was used to compare the differences between QDs treated cell data and control cell data. A p-value of < 0.05 was considered significant. All cell experiments were repeated in triplicate and the presented results show an average of three data sets. In each data set, approximately 1,000 cells were counted.

2.5 Microscopy

Live/dead staining using Trypan blue (Sigma, USA) was carried out on HeLa cells incubated with concentrations of 0, 50 nM/mL quantum dots. Cell images were taken in a phase contrast mode using Nikon TE2000-s microscope. Long-term live HeLa cell quantitative observation was undertaken on an Incucyte Kinetic Imaging System (Essen BioScience) at 10 × magnification. In this system, fluorescence and phase contrast images were collected every 30 minutes for 72 hours. Spectroscopic imaging was performed on a Zeiss LSM 710 laser scanning confocal microscope, equipped with 405 nm, 488 nm, 561 nm and 633 nm laser sources and a 34-channel QUASAR detector working in the lambda scanning mode.

Spectroscopic super-resolution data was collected through a $100 \times$ oil objective lens ($NA = 1.45$). Confocal pinhole was set at 1 Airy unit. Pixel size for scanning was set to 70 nm. Scanning speed was set at 3.15 $\mu\text{s}/\text{pixel}$ and rendered image were averaged from 4 scans in order to minimise background shot and read noise. Typically, the acquisition time was around 200 ms for a 256×256 image frame.

2.6 Algorithm implementations

Spectroscopic Super-resolution Algorithm (SSA) was developed in Matlab2014, on a 64-bit windows platform equipped with 2.1 GHz Intel Core i3 CPU. The overall framework of SSA starts from de-noising images frames, following by segmentation in which the regions of interest (ROI) are determined by the wavelength and objective numerical aperture. Then Gaussian fitting is applied to each ROI. SSA will repeat the fitting for all possible segmentations from 1 QDs to a possible maximum number (manually input) and select the best fits by evaluating and comparing the maximum likelihood value. A background image was used to initialise the threshold value for the de-noise process. Then a possible maximum QDs number in each frame was given manually according to the data. This number should be set as big as possible in order to cover all the possibilities. Other input such as, channel wavelength, raw image pixel size, render pixel size were initialised manually.

3. Results and discussion

3.1 Spectroscopic cell imaging

Technical implementations of spectroscopic confocal imaging can be realised in several ways [29]. The basic strategy is to spatially separate overall fluorescence signals by colour (i.e. emission wavelength). In practice this can be achieved using a confocal microscope capable of spectroscopic signal separation as illustrated in Fig. 1. For this purpose, readily available commercial systems can be used or adapted. In this study, we used Zeiss LSM 710 microscopy system on lambda scanning mode (in this mode, images were acquired displaying the intensity of the fluorescence probe within a spectral bandwidth of 10 nm, called the λ -stack).

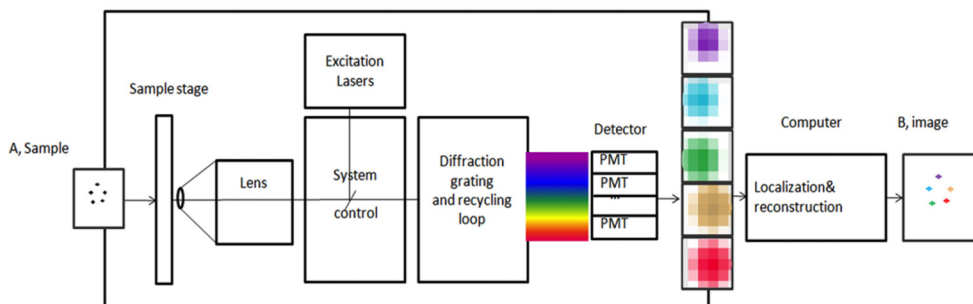


Fig. 1. Schematic view of spectroscopic super-resolution strategy. Sample 'A' is excited by a point laser source, then emission fluorescence is captured by the high NA lens and transferred into the microscope. Before being detected, this fluorescence light is recycled in a spectrophotometer which uses a diffraction loop to separates different wavelength components into different positions (showed as the rainbow bar before the PMTs detector). In other words, diffraction loop separates the closely-overlapping emission spectra of different quantum dots into different image frames, which is similar to the repeat photo-activation/imaging procedures in (f)PALM/STORM that separate overlapping fluorescence into different time series frames. Using this method, a super-resolution image 'B' is able to be reconstructed from separated image frames.

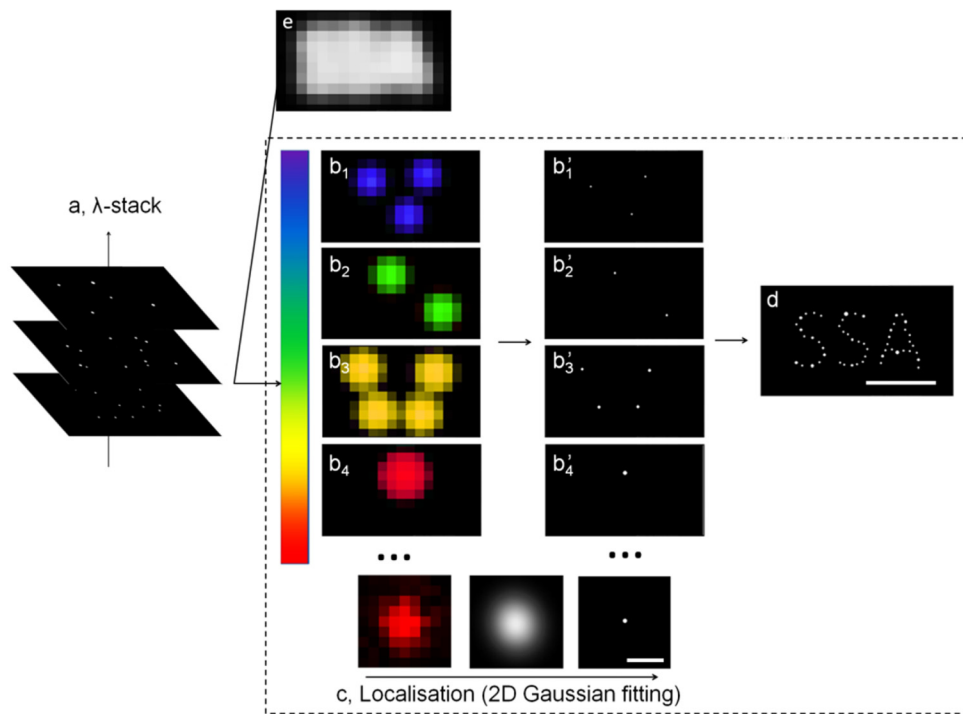


Fig. 2. Spectroscopic super-resolution reconstruction. (a) Individual planes of a spectral image series (λ -stack). The images were enlarged in b_1 – b_4 and then localised at a high precision (b'_1 - b'_4) using SSA algorithm based on Gaussian fitting (c). Super-resolution image (d) is obtained by putting all localisations together. However, fluorescence image without spectroscopic separation is shown as optical diffraction blurry (e). Scale bar, 200 nm (c), 400 nm (e).

In a typical spectroscopic imaging method (see Fig. 1), live cells (sample ‘A’) are labelled with fluorescence probes of different fluorescence emission wavelength. Fluorescence signals are spatially separated into different positions by wavelength. Spectroscopic super-resolution (SSR) can be further achieved by localising fluorescence probes (see Fig. 2) below Abbe diffraction limit in the spectroscopically separated channels instead of temporally (as done in STORM/PALM) [32,35].

3.2 QDs size dependent emission spectra

A good choice of the fluorescent probes (suitable small bio-imaging probes with distinguishable multi-spectra emission properties) is essential for efficient signal separation in SSR. Previously, super-resolution methods based on separation of spectroscopic components have been proposed using variety of dyes [9,31], however our approach has several advantages. We utilised the well-known and well-understood dependence of the peak emission wavelength on nanoparticle size in quantum confinement regime in semiconductor QDs. This approach has an additional advantage of using a single excitation wavelength for all QDs due to their wide absorption spectra. Three different sizes (5 nm, 11 nm and 15 nm in diameter, measured from TEM images) of commercial QDs (Qdot525, Qdot605, Qdot705) with different emission wavelengths (525 nm, 605 nm and 705 nm, Fig. 3(a)) were used in our test experiments. Measurements of the emission spectra of the QDs showed that individual QD had narrow emission spectrum (~30 nm FWHM, Fig. 3(a)). Correlative Light and Electron microscopy confirmed that small QDs (5 nm diameter) emit shorter wavelength light (525 nm wavelength), while larger QDs (11, 15 nm) corresponding to longer (605, 705

nm) emission wavelength as shown in Fig. 3(a). QDs size information was obtained by particle analysis from TEM images. Thus one can see that a random mixture of Qdot525, Qdot605, Qdot705 can be used for spectroscopic signal separation.

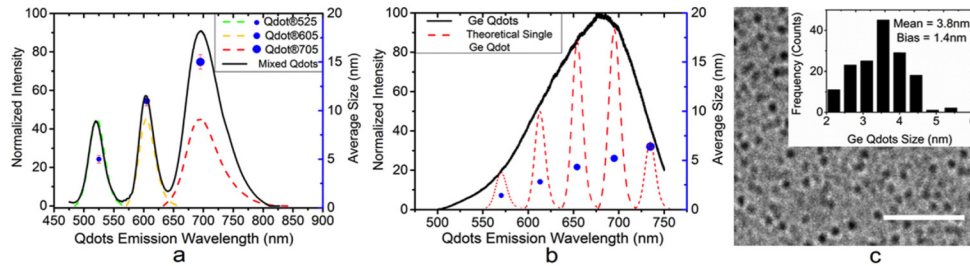


Fig. 3. Emission-size analysis for Invitrogen Qdots and Ge QDs. (a) Emission spectra of three Qdots (green, yellow, red dash lines) and their physical size (blue markers) measured from TEM images. Black full line is the emission spectra of an equally mixed sample of these three Qdots (5 nm Qdots emitting 515 nm light, 11 nm Qdots emitting 605 nm light, 15 nm Qdots emitting 705 nm light). Mixed sample shows a 3-peaks emission spectra ((black full line) contributed by three Qdots types. (b) A broad emission spectrum of as-prepared Ge QDs sample with particle sizes from 2.6 to 5.2 nm (c). It is assumed that emission is due to variation in particle sizes: red dash lines and blue markers indicate the emission spectra of several different size Ge QDs expected based on quantum confinement effects. (c) TEM image of Ge QDs. Scale bar, 50 nm.

Since the emission of QDs depends on particle size we can use the emission profile (see Figs. 3(a) and 3(b)) in a mixture for localisation of individual QDs. Here along with the standard Invitrogen Qdot systems we also used a novel form of colloidal Germanium QDs. Ge QDs were synthesised at room temperature and suspended in water. Taking into account the previously demonstrated size-dependent emission analysis, the emission spectra of the mixture of Ge QDs (~150 nm FWHM, black full line in Fig. 3(b)) indicates a broad size distribution due to multi-size QDs components (blue round markers in Fig. 3(b)) rendered with corresponding narrow spectra (red dashed lines in Fig. 3(b)). Additionally, Ge QDs were examined under a TEM at 50K magnification to obtain information about average size and size distribution. Ge QDs gave a probe size of below 5 nm (see Fig. 3(c)).

3.3 Fluorescence cell imaging and biocompatibility tests with Ge QDs

In order to evaluate suitability of Ge QDs as a fluorescence probe for cell imaging, we carried out both live and fixed cell tests to study the biocompatibility of QDs with HeLa cells. Each experiment was done in triplicate. As a start, to establish the effect of QDs on cell viability the Trypan Blue live dead test was performed on Qdot treated cells. We found a concentration QDs (50 nM / mL) did not obviously change the cell viability after 48 hours (Fig. 4(a) left). Additionally, both Ge QDs and Qdot treated live cells were continuously imaged (see Fig. 4(a) right) for 5 days in an Incucyte system. Using this live cell imaging system, we found that Ge QDs concentrations between 20 nM (0.146 mg/mL) to 500 nM (0.365 mg/mL) gave detectable fluorescence signals in cells while morphology and proliferation process of the cells were not visibly affected [36]. It's also well-known that QDs can cause DNA damage, which can be visualized using DAPI [37, 38]. DNA fragmentation and nuclear blebbing are indicative of apoptosis or necrosis. Hence, the analysis of nucleus is a way to assess the impact of QDs on cell viability. For this purpose, we analysed the DNA changes in cells while being treated with QDs. In preparation, HeLa cells in growth medium of 1 mL/well in a 12-well plate at a density of 5000 cells/mL were used. Next 25 nM growth medium, Ge QDs, Qdot625 solutions were added to the three wells. Cells were then fixed and stained with DAPI (see Fig. 4(b)) followed by quantitative analysis of the nucleus shape (see

Fig. 4(c)). There were no visible detrimental effects and DNA fragmentation with seeding Ge QDs into HeLa cells, which is consistent with our previous studies [36].

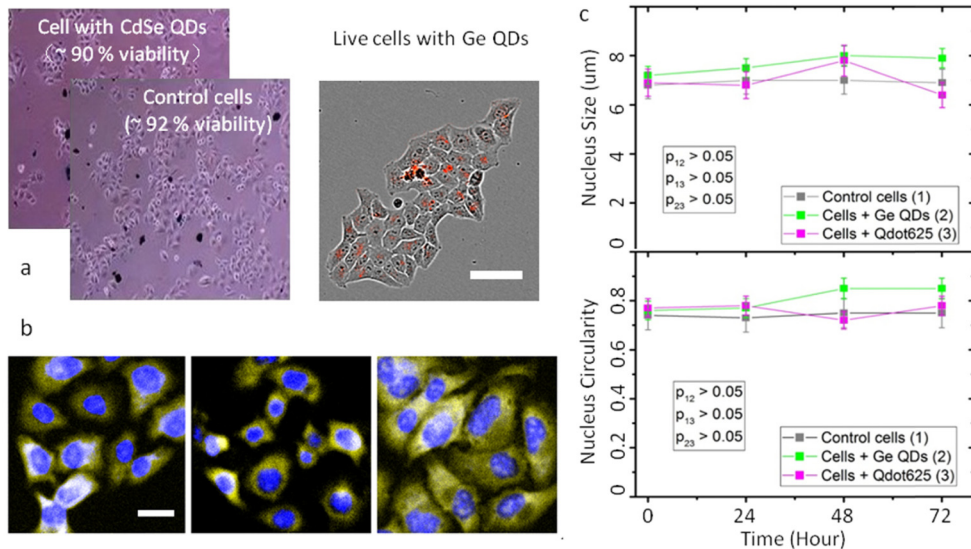


Fig. 4. Biocompatibility tests of Ge QDs and Invitrogen Qdots on HeLa cells. (a) Left, Trypan blue test of Qdots (50 nM/ mL) treated Hela cells. Right, merged phase contrast & fluorescence images of Ge QDs in live cells. (b) DNA staining of HeLa cells treated by, Left, non-QDs, Middle, Ge QDs (25 nM / mL), Right, Invitrogen Qdots (25 nM / mL) after 24 hours. (c) Quantitative analysis of cell nucleus size (top) and shape (bottom) changes under QDs treatments. Results are presented as mean and standard deviation. A p value of larger than 0.05 ($p > 0.05$) is considered non-significant statistic difference between the compared data sets. Scale bar, 30 μm (a), 20 μm (b).

Following statistical analysis of the data all p-values in the t-tests were found to be larger than 0.05 (see Fig. 4(c)). This means that three different treatments have shown non-significant statistical differences in nucleus size and circularity. When compared with control treatment, all QDs had very little impact on the shape and size of the cell nucleus over the reported time frames with Ge QDs showing slightly better performance than Invitrogen Qdots625. This is not unexpected as Ge QDs should deliver improved biocompatibility compared to that of Invitrogen Qdots (based on CdSe/ZnS technology) as has been also shown in our previous work [36].

3.4 Spectroscopic cell imaging using Qdot and Ge QDs

As proof-of-principle of SSR method, spectra imaging was initially carried using Invitrogen Qdots. HeLa cells were non-specifically labelled with the mixture of Qdots described previously and the total fluorescence emission image (sample excited by 488 nm laser light, and the emission was recorded between 498 nm to 721 nm) is presented in the inset in Fig. 5(a). We selected a small area of interest (see Fig. 5(b), also marked as yellow square corresponding to a 1.5 $\mu\text{m} \times 1.5 \mu\text{m}$ area in Fig. 5(a)). This image consists of a sum total of 33 spectroscopically separated image frames (33 channels λ -stack, Fig. 5(c)). These λ -stack frames contain specific unique fluorescence information from each of the 10 nm spectral width channel. Thus, three channels (shown in green, magenta, yellow, Fig. 5(c)) corresponding to the emission peaks of Qdots are selected to run localisation algorithms to reconstruct a higher resolution image following imaging of QDs. The λ -stack frames were captured during a single scanning period, which took 3.15 μs for a pixel and about 200 ms for a 256 \times 256 size image.

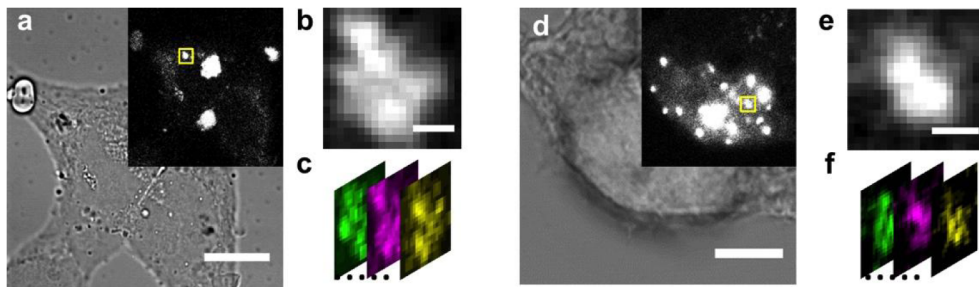


Fig. 5. Spectroscopic cell images. (a) HeLa cell cultivated with mixed three Invitrogen Qdots and total fluorescence image. (b) Zoomed view of the yellow square area in the fluorescence image (a) and the spectroscopic separated image frames – (c) Lambda stack collected using confocal microscopy. Three channels (517nm, 605nm, 702nm) where three Qdots emission peaks occur were presented (green, magenta and yellow). Each frame only contains fluorescence signals from specific Qdots thus generate a unique fluorescence image. (d) Ge QDs labelled HeLa cell was demonstrated using the same microscopy technique. Ge QDs shows a strong fluorescence emission in cells. (e) Zoomed view of details of the yellow square in the fluorescence image (inset d) and f indicates the spectroscopic separated images frames. Three channels (595 nm, 644 nm, 692 nm) present the different spectroscopic images. (f) Lambda stack frames contain different spectroscopic fluorescence signals individually, therefore generate different images. Scale bars, 10 μm (a), 5 μm (d) 500 nm (b, e).

A similar approach was used for spectroscopic super-resolution microscopy using HeLa cells labelled with Ge QDs. HeLa cells were cultivated with Ge QDs for 24 hours and the sum fluorescence image is shown in the inset in Fig. 5(d). Similarly, a small area of interest (see Figs. 5(e) and 5(f), also marked as the yellow square in Fig. 5(d)) was selected to test spectroscopic localisation algorithms. For demonstration of the SSR, 3 channels \sim 50 nm apart were selected from 33 channels λ -stack for further processing. Differences between the selected colour (wavelength) channels become apparent even before the processing stage in both Qdot cell data (see Fig. 5(c)) and Ge cell data (see Fig. 5(f)).

An important issue associated with these spectroscopic separation imaging is the spectra overlap of similar size quantum dots. With multiple QDs where close spectral bands (for example 10 nm width in our case) are present, it is often not possible to fully isolate signals from individual QDs. Thus the individual spectral channels usually contain fluorescence light originating from several QDs, which have to be separated by computational methods such as spectral unmixing or emission fingerprinting [39]. In this techniques, the fluorescence contributions of different QDs at a given pixel are calculated based on the spectral information. In mathematical realisation, this is done by the inversion of a linear equation combining the fluorescence molecule concentration, the fluorescence signal intensity and a coefficient term revealing the emission spectra properties of the molecules. In principle, optimised resolution could be expected through spectra unmixing even under presence of a relatively high noise level. Spectral unmixing was not carried in our demonstration because the three selected spectral channels locate farther apart than a single QD spectral FWHM (\sim 45 nm [40]).

3.5 Localisation algorithm and super-resolution reconstruction

For an optimal resolution in localisation it is necessary to strike a balance between raw data processing steps and localization precision. Additionally, particular consideration should be taken on the variation of PSFs in different channels, which demands individual processing of each frame. Previously we compared several available image processing algorithms capable of delivering super-resolution images [10]. However, since the method here relies on improvement of resolution via the wavelength of emitted light from differently sized probes rather than switching of a probe between light and dark state they are not relevant for this analysis.

As a result, we developed a Matlab algorithm - Spectroscopic Super-Resolution Algorithm (SSA) - to handle the SSR microscopy data for localisation and reconstruction. The SSA includes three parts: de-noising, segmentation and maximum likelihood estimation (MLE) [41]. The de-noising step employed a Gaussian de-noise model and Poisson de-noise model (one should choose the appropriate model based on the detector specification). For our PMT detected image data, the Gaussian de-noise model was used. The de-noising is achieved through a convolution process. The degree of de-noise is determined by the standard deviation of the Gaussian distribution of the noise [42], where larger standard deviation Gaussians require larger convolution kernels. The grey value of a pixel v_{xy} is replaced by a weighted average of its neighbourhood x,y,v as shown in Eq. (1).

$$v = \frac{1}{2\pi\sigma^2} e^{-\frac{x^2+y^2}{2\sigma^2}} \cdot v_{xy} \quad (1)$$

where σ stands for the standard deviation of Gaussian distribution of the noise.

The segmentation step is to partition the original image into multiple segments, which satisfies the hard constraints of the possible sizes of PSF. Firstly, the grey value to each pixel is acquired and the pixel with a largest grey value is identified. The area around this pixel (ROIs) is selected based on expected PSF size. Then, a pixel with the next largest grey value is selected and procedure is repeated until the whole image is segmented. The resulting segments collectively cover the entire image and each of them includes a brightest point and its neighbourhood pixels in the constrained region.

MLE was implemented to achieve the Gaussian fitting for PSF in the ROIs. Then the mean and variance of the Gaussian functions can be estimated with MLE. Mathematically, this is achieved by treating the mean and variance as variables and finding particular parametric values that maximise the likelihood function (making the observed results the most probable). For a data set D , the likelihood for how D matches the Gaussian distribution $N(\mu, \sigma^2)$ is judged using equation Eq. (2).

$$f(D|\mu, \sigma) = \frac{1}{\sqrt{2\pi}\sigma} e^{-\left[\sum_{i=1}^n (d_i - \mu)^2\right]} \quad 0 < d_i < \infty \quad (2)$$

There are two parameters (μ, σ) to be determined. Hence, we maximise the likelihood $f(D|\mu, \sigma)$ over both parameters simultaneously. Since the logarithm $\log f(D|\mu, \sigma)$ is a continuous strictly increasing function over the range of the likelihood, set $0 = \frac{\partial f(D|\mu, \sigma)}{\partial \mu}$

and $0 = \frac{\partial f(D|\mu, \sigma)}{\partial \sigma}$, we get:

$$\begin{aligned} \mu &= \frac{\sum_{i=1}^n d_i}{n} \\ \sigma &= \sqrt{\frac{\sum_{i=1}^n (d_i - \mu)^2}{n}} \end{aligned} \quad (3)$$

where μ determines the localisation position and σ accounts for the error and localisation confidence. Once the localisations have been determined, the output figure is then reconstructed. Molecule positions are printed with standard plot function in Matlab2014 with default black colour.

In our SSR reconstruction process of the data of HeLa cells with QDs, individual ROI size was tailored according to the changes of PSF with wavelength (the default fitting region size was set as 3 times the PSF size in each channel) and the default value of 3 was used. The maximum possible number of QDs in each frame was set at 1000 according to an initial guessing by looking at the raw image. It took less than one second for SSA to process each frame. As a reference, we ran a similar algorithm developed to handle STORM data (csSTORM [43]) on our images. In the csSTORM reconstruction, the processing parameters were set as default (optimisation chi square value of 1.5 and the baseline offset of the camera at 100). Processing time in csSTORM was about 10 seconds for each frame.

Figure 6 shows the results of analysis of Qdot data (left side) and of Ge QDs data (right side). Selected image frames and the sum images in Fig. 5 are used here (see Figs. 6(a)-6(d)). CSSTORM-processed results can be seen in (e) to (j), and the final reconstructed image (g, j) is obtained by merging frames in (f, i). SSA-processed results are represented in (k) to (n). The SSA localisations are filtered by a hard constraint that the Gaussian fitting confidence of larger than 95%. This parameter is not seen in csSTORM as it doesn't return any localisation confidence. SSA reconstruction spots size was set as 12 nm for Ge QDs data and 40 nm for Qdots data (twice the size of the physical size of Qdot). In such case, one would expect more Ge QDs to be localised than Qdots for a non-Nyquist-limited sample, because smaller reconstruction spot sizes allow SSA algorithms potentially localise more QDs in a specific area. This is also proven in the reconstruction results (16 QDs in (n) while 12 in (i)). As a most significant difference, both SSA and CSSTORM return more localisations with spectroscopic data than that of non-spectroscopic data and there is a three-folder improvement (45 QDs in (g) while 8 in (e), 44 in (j) while 9 in (h), 12 in (i) while 4 in (k), 16 in (n) while 5 in (m)). With the combination of using ultra-small Ge QDs and spectroscopic imaging method, we have obtained a comprehensive four-folder improvement in the number of localizations (16 in (n) comparing to 4 in (k)). Some of these improvements are, no-doubt, due to the small size of Ge QDs (2-5 nm) compared to Invitrogen Qdots (5-15 nm). Also some improvements in the localisation number and precision come in part from SSA algorithm, which delivers better results than csSTORM. This algorithm reduces the unnecessary processing steps of raw data and pays greater attention to extracting useful information in a single frame, instead of increasing the speed for multi-frames processing.

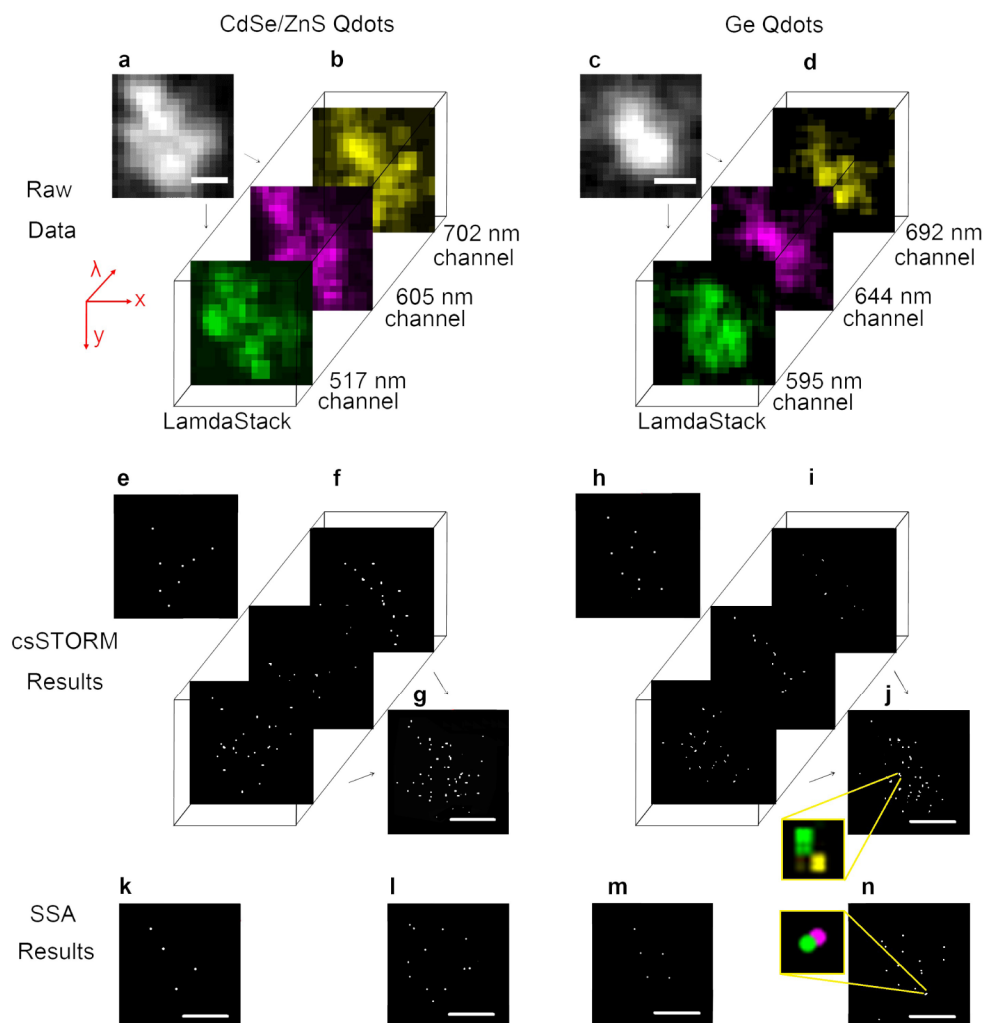


Fig. 6. Spectroscopic super-resolution localisation and reconstruction. Left column are Qdots super-resolution data and results. (a, b) selected three spectroscopic separated frames (595 nm, 644 nm, 692 nm) and sum of all spectroscopic separated frames. (e, f) csSTORM localised results of (a) and (b) respectively; (g) final merged csSTORM results of images from (f). (k, l) localisation and reconstruction of (a, b) frames using our SSA algorithm, revealing the potential Qdots distribution behind the fluorescence signals (a). Right column are Ge QDs data and results. (c, d) fluorescence and sum images. (h-j) csSTORM process results, a final csSTORM final result (j). (m, n) SSA result of (c, d) represents the final super-resolution image in SSRM. Two closely located QDs (yellow zoom-in square in (i) and (n)) are localised through spectroscopic separation and reconstruction. Scale bars, 500 nm.

Considering the real QDs distribution and the effective resolution of the super-resolution images, it is possible that several identical QDs may be located too close to each other (less than 5 nm for Ge QDs for example), this could reduce accuracy of single molecule localisation because these QDs would be regarded as one QD. This means that the localisations could be further supplemented with a standard fitting error (typically from 10 to 30 nm in FWHM). Furthermore, the registered QDs number will also be influenced by the initial guessing of maximum possible number which is user determined. To any existing data, the maximum number could be estimated by using the total intensity grey value divided by the intensity one single QDs, for example, 100 Ge QDs (intensity grey of 600 for single QD)

in a region with total intensity grey value of 60000. Higher density of QDs than this number will lead to the SSA algorithm not suitable to the data any more. In this context, further improvement to the algorithm can be developed to achieve a balance between the QDs labelling density and the effective resolution.

The localised QDs numbers and distributions will, of course, also depend on the labeling conditions of the biological epitope. In our proof-of-principle case, we load QDs into cells by cell endocytosis in non-specific labeling. Direct assessment of labelling density, QD distribution and their effect on resolution can be done using correlative light and electron microscope imaging that can directly visualise QDs. As an alternative, the Fourier Ring Correlation analysis has been widely used to measure the effective resolution, but the method is based on computational analysis only [44]. Other direct experimental methods such as DNA rulers and DNA origami can also potentially yield the effective resolution of a super-resolution imaging method.

4. Conclusions

Here we proposed QD-based ‘spectrally assigned’ localisation method for super-resolution microscopy. This approach allows to utilise a conventional confocal microscope capable of spectral signal separation (e.g. Leica TCS SP, Zeiss LSM 701 with QUASAR detector etc.), which when coupled with a novel probe (Ge QDs) and a customised algorithm (SSA). In fact, any conventional microscope equipped with a spectroscopic detector is suitable for our method. Furthermore, it has a potential to deliver data acquisition rates on ms scale thus potentially providing super-resolution in live systems. Compared to temporal separation in stochastically reconstructed super-resolution microscopy (for example, the stochastic super-resolution imaging based on QDs blinking statistics), the shorter data acquisition time in spectra separation microscopy greatly reduces the demand of system drift correction and environment influence compensation. The main challenges of this method are labelling density control and preparation of suitable QD mixture. In order to obtain well-spectrally separated images a randomly mixed multi-size QDs and a uniform labelled sample are desirable. Further research is required into the effect of the labeling density and QD mixtures on the resolution delivered by this method, as well as live cell super-resolution imaging and 3D imaging.

Funding

QMUL/CSC scholarship (2011611045); BBSRC grant (BB/J001473/1).

Acknowledgments

We thank Dr Katy Allen and Dr Merewyn Loder for technical assistance with confocal imaging. Dr Rosy Manser and Dr Nicolas Sergeant (Carl Zeiss) for constructive discussions and Dr John Connelly and Essen Bioscience for assistance with the Incucyte.